# Molecular-level nucleation mechanism of iodic acid and methanesulfonic acid

An Ning[1], Ling Liu[1], Lin Ji[2], and Xiuhui Zhang[1]

[1]Key Laboratory of Cluster Science, Ministry of Education of China, School of Chemistry and Chemical Engineering, Beijing

5  Institute of Technology, Beijing 100081, China

[2]Department of Chemistry, Capital Normal University, Beijing 100048, China

*Correspondence to*: Xiuhui Zhang (zhangxiuhui@bit.edu.cn)

**Abstract.** Both iodic acid ($HIO_3$, IA) and methanesulfonic acid ($CH_3S(O)_2OH$, MSA) have been identified by field studies as important precursors of new particle formation (NPF) in marine areas. However, the mechanism of NPF in which IA and MSA

10  are jointly involved is still unclear. Hence, we investigated the IA-MSA nucleation system under different atmospheric conditions and uncovered the corresponding nucleating mechanism at the molecular level for the first time, using quantum chemical approach and Atmospheric Cluster Dynamics Code (ACDC). The findings show that the pure-IA nucleation rate was much lower than the results of CLOUD experiments. MSA can promote IA cluster formation through stabilizing IA via both hydrogen and halogen bonds, especially under conditions with lower temperatures, sparse IA and rich MSA. However, the

15  nucleation rate of the IA-MSA mechanism is much lower than that of field observation, indicating that the effect of additional nucleation precursors needs to be considered (e.g., $H_2SO_4$, $HIO_2$, $NH_3$ and amines). The IA-MSA nucleation mechanism revealed in this study may help to gain insight into the joint effect of marine sulfur- and iodine-containing components on marine NPF.

## 1 Introduction

20  Marine aerosols, being the primary natural aerosol system (O'dowd and De Leeuw, 2007), significantly affect global radiation balance and climate by regulating cloud properties as cloud condensation nuclei (CCN) (Takegawa et al., 2020; IPCC, 2013). Nearly half of the CCNs originate from the new particle formation (NPF) via the gas-to-particle conversion (Merikanto et al., 2009; Yu and Luo, 2009). As a major source of CCN globally, NPF mainly consists of the nucleation of gaseous molecules and the subsequent growth of the formed clusters (Kulmala et al., 2013; Kulmala, 2003; Zhang, 2010). Although extensive

25  studies have provided observational evidence of NPF events in the coastal zone, open ocean, and even ice-covered polar regions (Zheng et al., 2021; Sipila et al., 2016; Yu et al., 2019; Baccarini et al., 2020), the corresponding NPF mechanisms at the molecular level remain poorly understood stemming from the lack of chemical speciation in the initial nucleating steps.

Marine NPF, particularly in remote marine areas, is more affected by biological emissions compared to inland ones with anthropogenic influence (Kerminen et al., 2018). Historically, sulfur-containing species originating from ocean-emitted

30    dimethyl sulfide (DMS) have long been identified as significant components of marine aerosols (Charlson et al., 1987; Shaw, 1983; Bates et al., 1992). Methanesulfonic acid (CH₃S(O)₂OH, MSA), as a well-known oxidation product of DMS (Chen et al., 2018; Hatakeyama et al., 1982), is widely dispersed throughout the world's oceans and has considerable atmospheric concentrations (Chen et al., 2018), comparable to or higher than sulfuric acid (SA), [MSA]/[SA] = 10% −250% (Berresheim et al., 2002; Davis et al., 1998; Eisele and Tanner, 1993). Moreover, MSA has been experimentally demonstrated to be a

35    significant nucleating precursor in coastal and remote oceans (Dawson et al., 2012; Hodshire et al., 2019; Karl et al., 2007). Along with stricter global controls on anthropogenic SO₂ emissions, the impact of MSA on NPF will become increasingly significant in the future (Perraud et al., 2015), particularly in marine areas.

In addition to the above sulfur precursors, recent experimental and theoretical studies (He et al., 2021; Martín et al., 2020; Xia et al., 2020; Rong et al., 2020) have also recognized the critical role of iodine compounds in marine NPF process.

40    According to the field studies (O'dowd et al., 2002; Sipila et al., 2016), the observed intense NPF events occur during low tide and are accompanied by a significant increase in iodic acid (HIO₃, IA) concentration in the coastal Mace Head, indicating that the coastal NPF is primarily driven by subsequential addition of IA and involves the participation of I₂O₅. More recently, He et al. (2021) demonstrated experimentally that, in addition to IA and I₂O₅, iodous acid (HIO₂) and I₂O₄ are also involved in the cluster formation process, with HIO₂ playing a key role in the stabilization of neutral IA clusters. Also, recent evidence suggests

45    that the NPF events in the sea-ice covered Arctic region are also mainly driven by IA (Baccarini et al., 2020). Notably, in addition to IA, significant concentrations of MSA were observed during marine NPF events (Beck et al., 2021). Although MSA and IA were detected in the smallest clusters (Beck et al., 2021), it is still unknown whether they could be simultaneously involved in the early nucleation process. If so, their joint nucleation mechanism and the corresponding regions affected by that mechanism need be further elucidated.

50    Herein, the high-level quantum chemical calculations combined with Atmospheric Clusters Dynamic Code (ACDC) (Mcgrath et al., 2012) were employed to simulate the nucleating process of the (IA)$_x$·(MSA)$_y$, ($0 \leq x \leq 6$, $0 \leq y \leq 3$, $1 < x + y \leq 6$) system. Under different atmospheric conditions (temperature and precursor concentration), a series of ACDC simulations were carried out to explore: i) the binding nature of IA and MSA, ii) the joint effects of IA and MSA on the nucleation, iii) which conditions are more affected by the IA-MSA mechanism. The current work may contribute to developing a more

55    comprehensive marine NPF mechanism and explaining some missing sources of particles in marine environments.

## 2 Methods

### 2.1 Quantum chemistry calculation

All structure optimizations with tight convergence criteria and frequency calculations with density function theory (DFT) were carried out by Gaussian 09 package (Frisch et al., 2009). Considering the variety of possible isomers of multimolecular clusters,

60    a systematic multi-step conformation search was employed here to locate the lowest-energy cluster structures. The structures

of the pure-IA clusters employed in this study were referred to the study of Rong et al., (2020). A new $(IA)_6$ cluster with lower energy was found here. For each studied IA-MSA cluster, the artificial bee algorithm combining the UFF force field (Rappé et al., 1992) was adopted to yield 1000 initial configurations from 5000 generations by ABCluster software (Zhang and Dolg, 2015). After pre-optimization by the PM7 semi-empirical method (Stewart, 2013) with MOPAC2016 (Stewart, 2016), the 100 structures with lower energies were left for further optimization at $\omega$B97X-D/6-31+G* + Lanl2DZ (for iodine) level of theory due to the best performance of $\omega$B97X-D functional in studying atmospheric clusters (Elm and Kristensen, 2017; Schmitz and Elm, 2020). The final global minima were reoptimized by $\omega$B97X-D functional with 6-311++G(3df,3pd) (Francl et al., 1982) basis set for H, C, O and S atoms, and aug-cc-pVTZ-PP with ECP28MDF for I atom (Peterson et al., 2003) and were identified with the lowest Gibbs formation free energy ($\Delta G$). It is noteworthy that the larger aug-cc-pVTZ-PP basis set (for iodine) was employed in the present study compared to the aug-cc-pVDZ-PP basis set (for iodine) in our previous work (Rong et al., 2020), because higher level of theory usually implies a better calculation accuracy.

The single-point correction was further performed by RI-CC2 method (Hattig and Weigend, 2000) with aug-cc-pVTZ (for H, C, O) + aug-cc-pV(T+d)Z (for S) + aug-cc-pVTZ-PP with ECP28MDF (for I) basis set using Turbomole program (Dunning et al., 2001; Ahlrichs et al., 1989), since the ACDC simulations based on RI-CC2 values are in good agreement with the experimental results (Lu et al., 2020; Kürten et al., 2018; Li et al., 2020; Almeida et al., 2013). Herein, in this work, the Gibbs formation free energies ($\Delta G$, kcal mol$^{-1}$) of the studied clusters were calculated as Eq. (1):

$$\Delta G = \Delta E_{\text{RI-CC2}} + \Delta G_{\text{thermal}}^{\omega\text{B97X-D}} \tag{1}$$

where $\Delta E_{\text{RI-CC2}}$ is the electronic contribution and $\Delta G_{\text{thermal}}^{\omega\text{B97X-D}}$ is the thermal contribution to Gibbs free energy. For subsequent clustering kinetic simulations at different temperatures, the $\Delta G$ of clusters ranging from 218 K to 298 K were calculated by Shermo 2.0 (Lu and Chen, 2021) and collected in Table S3.

## 2.2 Wavefunction analysis

To better understand the interactions between IA and MSA, the bonding nature was investigated through wave function analysis using Multiwfn 3.7 (Lu and Chen, 2012). Specifically, the molecular electrostatic potential (ESP) was calculated for IA and MSA, which facilitates understanding their potential interaction sites. Moreover, the natural bond orbital (NBO) analysis (Reed et al., 1988) was carried out to give a detailed insight into intermolecular interactions. Based on the final identified stable clusters, the NBO information calculated by Gaussian 09 is resolved by Multiwfn and the key interactive orbitals are visualized by VMD 1.9.3 (Humphrey et al., 1996). To further quantify the binding strength, electron density $\rho(r)$, Laplacian electron density $\nabla^2\rho(r)$, energy density $H(r)$ at corresponding bond critical points (BCPs) based on atoms in molecules (AIM) theory (Becke, 2007; Lane et al., 2013) were also calculated in this work (Table S1 in ESI).

## 2.3 Atmospheric cluster dynamic simulations

Simulation of the nucleation process of the IA-MSA system is achieved by the Atmospheric Clusters Dynamic Code (ACDC) (Mcgrath et al., 2012). Specifically, the ACDC derives the steady-state concentration and cluster formation rates by solving the birth-death equations (Eq. (2)).

$$\frac{dc_i}{dt} = \frac{1}{2}\sum_{j<i}\beta_{j,(i-j)}C_jC_{(i-j)} + \sum_j\gamma_{(i+j)\to i}C_{i+j} - \sum_j\beta_{i,j}C_iC_j - \frac{1}{2}\sum_{j<i}\gamma_{i\to j}C_i + Q_i - S_i \tag{2}$$

where $C_i$ refers to the cluster $i$ concentration, $\beta_{i,j}$ is the collision rate coefficient between clusters $i$ and $j$, $\gamma_{i\to j}$ is the evaporation rate coefficient of smaller cluster $j$ from the parent cluster $i$, $Q_i$ and $S_i$ are the outside source and loss term of cluster $i$, respectively. $\beta_{i,j}$ is calculated based on the kinetic gas theory, which is given as:

$$\beta_{i,j} = \left(\frac{3}{4\pi}\right)^{1/6}\left(\frac{6k_BT}{m_i} + \frac{6k_BT}{m_j}\right)^{1/2}\left(V_i^{1/3} + V_j^{1/3}\right)^2 \tag{3}$$

where $V_i$ and $m_i$ are the volume and mass of cluster $i$, respectively. $k_B$ is the Boltzmann constant, and $T$ is the temperature. Eq.(3) is derived from the hard-sphere collision theory where $V_i = 3/4 \times \pi \times (D_i/2)^3$. The diameter $D_i$ of cluster $i$ is calculated by Multiwfn (Lu and Chen, 2012). Evaporation rate coefficients $\gamma_{(i+j)\to i,j}$ are derived from $\Delta G$ of clusters and the corresponding collision rate coefficients based on the detailed balance assumption (Mcgrath et al., 2012):

$$\gamma_{(i+j)\to i,j} = \beta_{i,j}\frac{P_{ref}}{k_BT}\exp\left(\frac{\Delta G_{i+j} - \Delta G_i - \Delta G_j}{k_BT}\right) \tag{4}$$

where $P_{ref}$ is the reference pressure (1 atm) at which the Gibbs free energies were determined, and $\Delta G_i$ is the Gibbs formation free energy of the formation of cluster $i$ from the corresponding monomers.

In the present study, the ACDC simulations only modelled the neutral cluster formation process and did not consider the charge, nor the effect of water. Since IA is weakly bound to water, it is less inclined to exist as hydration of IA in tropospheric conditions (Khanniche et al., 2016). Meanwhile, the nucleation efficiency of MSA and water is low (Arquero et al., 2017). Thus, the effect of water on the conclusion in this study is limited. The settings of the boundary conditions of the ACDC simulations are discussed in Section S1 (ESI) and summarized in Table S5.

## 3 Results

### 3.1 Cluster conformational analysis

The obtained most stable structures of $(IA)_x \cdot (MSA)_y$ ($0 \leq x \leq 6$, $0 \leq y \leq 3$, $1 < x + y \leq 6$) clusters are presented in Fig. S1 and the corresponding Cartesian coordinates are collected in Table S7 in the supplement. To investigate the intermolecular bonding potential of IA and MSA, the electrostatic potential (ESP) was calculated to analyse their potential interaction sites.

As shown in Fig. 1a, IA has positive ESPs (red region) surrounding its -OH group, with a maximum value of +59.04 kcal

mol$^{-1}$, making the -OH group an effective hydrogen bond (HB) donor. And IA's two terminal oxygens with negative ESPs (-29.09 kcal mol$^{-1}$ and -29.47 kcal mol$^{-1}$) can serve as HB acceptors. Similarly, the -OH group of MSA has the strongest electrophilicity (ESP value of +63.86 kcal mol$^{-1}$) as the HB donor, while its terminal O atom has strong nucleophilicity as the HB acceptor, due to its lone pair of electrons. In this case, IA and MSA can directly bind with each other via HBs. Moreover, IA possesses positive charge localization (the so-called $\delta$-hole) with a maximal ESP value of +51.87 kcal mol$^{-1}$ at the end of the iodine atom along the O-I direction. This electron deficient region tends to attract the electron-rich oxygen atom of the MSA to form the halogen bonds (XB) O-I···O (green band line in Fig. 1a). From the skeletal formula presented in Fig 1. (a), we can know that a formed (IA)$_1$·(MSA)$_1$ cluster is stabilized by both HB and XB. The similar situation has also been found in the larger IA-MSA clusters in Fig. S1.
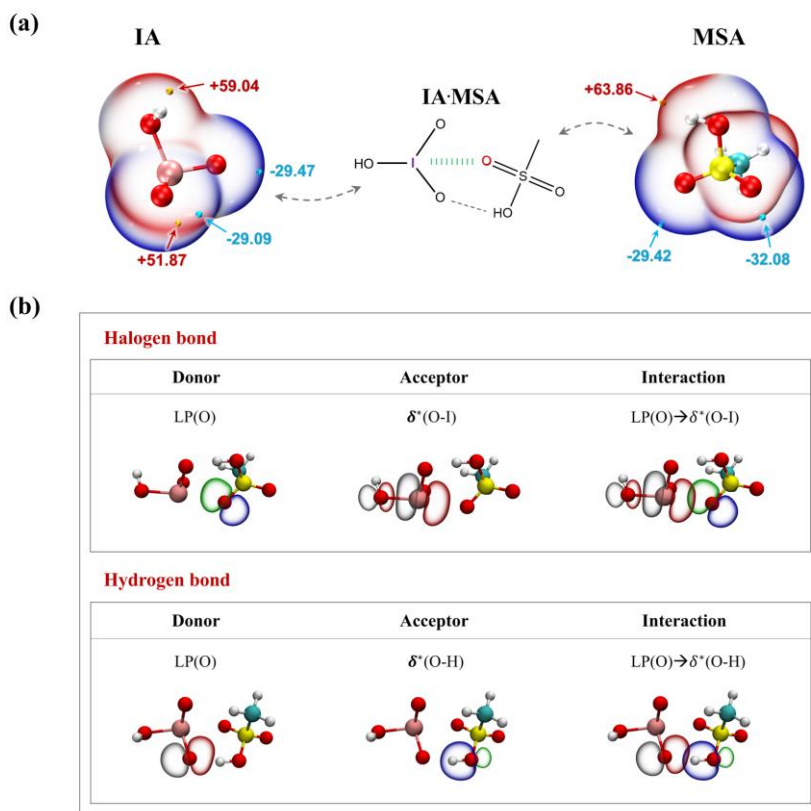
**Figure 1. (a)** The ESP-mapped molecular vdW surfaces of iodic acid (IA) and methanesulfonic acid (MSA). The pink, red, yellow, cyan, and white spheres represent I, O, S, C, and H atoms, respectively. The yellow and cyan dots indicate the positions of maximums and minimums of ESP in kcal mol$^{-1}$, respectively. **(b)** The donor–acceptor NBOs involved in the (IA)$_1$·(MSA)$_1$ cluster. LP indicates the lone-pair orbitals, and $\delta^*$ indicates the antibonding orbitals.

Additionally, as illustrated in Fig. 1b, the natural bond orbital (NBO) analysis was performed to reveal the bonding nature of IA and MSA. For the formed O-I···O halogen bond, the lone-pair orbitals LP(O) in the terminal oxygen atom of MSA acts

as an electron donor, while the antibonding orbital $\delta^*$(O-I) in IA is the electron acceptor. Essentially, halogen bonding originates from the interactions between LP(O) and $\delta^*$(O-I) orbitals, accompanied by intermolecular charge transferring from LP(O) to $\delta^*$(O-I). In the case of the O-H$\cdots$O hydrogen bond, the LP(O) of IA serves as the donor orbital and $\delta^*$(O-H) of MSA is the acceptor orbital, and the charge shifts from LP(O) to $\delta^*$(O-H). The ESP and NBO results indicate that IA and MSA are capable of forming both HB and XB and have the potential to form stable clusters.

To quantify the bonding strength of HBs or XBs within the studied IA-MSA clusters (Fig. S1 in ESI), the bonding properties including electron density $\rho(r)$, Laplacian electron density $\nabla^2\rho(r)$ and energy density $H(r)$ at the bond critical points (BCPs), are calculated based on AIM methodology (Becke, 2007; Lane et al., 2013) and collected in Table S1. For O-I$\cdots$O XBs, the $\rho(r)$, $\nabla^2\rho(r)$ and $H(r)$ values at the BCPs are in the ranges of $0.0143 - 0.0849$, $0.0409 - 0.1589$, and $-0.0265 - 0.0019$ a.u., respectively. As to O-H$\cdots$O HBs, the $\rho(r)$, $\nabla^2\rho(r)$ and $H(r)$ values at the BCPs are in the ranges of $0.0178 - 0.0796$, $0.0615 - 0.1141$, and $-0.0032 - -0.0332$ a.u., respectively. The electron density $\rho(r)$ is generally positively correlated with the bond strength, and the $\rho(r)$ values (Table S1 in ESI) are well within the specified $\rho(r)$ range of HBs ($0.002 - 0.040$ a.u.) (Grabowski, 2004; Koch and Popelier, 1995) indicating that all the O-H$\cdots$O non-covalent interactions are indeed HBs. Moreover, according to the classification of HBs (Rozas et al., 2000), all the HBs formed within IA-MSA clusters are medium HBs ($12.0 < E$ (interaction energy) $< 24.0$ kcal mol$^{-1}$) with $\nabla^2\rho(r) > 0$ and $H(r) < 0$. Overall, the conformational analysis suggests that MSA can stabilize IA clusters by forming relative strong non-covalent interactions such as HBs and XBs, and thus has the potential to form relatively stable clusters with IA.

## 3.2 Cluster stability analysis

To evaluate the thermodynamic stability of formed IA-MSA clusters, the Gibbs formation free energy ($\Delta G$, kcal mol$^{-1}$) of each studied $(IA)_x \cdot (MSA)_y$ ($0 \leq x \leq 6$, $0 \leq y \leq 3$, $1 < x + y \leq 6$) clusters at $T = 218$ K $- 298$ K ranging from boundary layer to free troposphere (Williamson et al., 2019) and $p = 1$ atm were calculated by Eq. (1) and shown in Table S3. In the present study, the analysis and discussion of the simulation results are mainly at $T = 278$ K.

As shown in Fig. 2a, the $\Delta G$s of IA-MSA clusters at 278 K decrease with the increasing of cluster size, indicating that the cluster growth process is energetically favourable. And the same trend is also observed at 298 K (Fig. S2) and 258 K (Fig. S3). The $\Delta G$ of the $(IA)_x \cdot (MSA)_1$ ($x = 1 - 5$) clusters, are $7.71 - 15.67$ kcal mol$^{-1}$ lower than that of the corresponding $(IA)_x$ clusters, indicating that pure-IA clusters could potentially grow up by binding with MSA. Moreover, the corresponding total evaporation rate coefficients ($\sum\gamma$, s$^{-1}$) of clusters were calculated at 278 K by Eq. (4) and presented in Fig. 2b and Table S4. In general, a lower $\sum\gamma$ value indicates greater cluster stability. As shown in Fig. 2b, the $\sum\gamma$ of larger clusters, $(IA)_{4-6}$ and $(IA)_{3-4} \cdot (MSA)_2$, are significantly lower than those of the corresponding initial small-sized clusters, indicating that the stability increases during the cluster growth. Considering the competition between collision and evaporation during the clustering process, the ratio of collision frequencies versus total evaporation rate coefficients ($\beta C / \sum\gamma$) was calculated to access the probability of cluster growth. If $\beta C / \sum\gamma > 1$, further growth of cluster colliding IA or MSA molecules can be assumed to dominate over cluster

evaporation (details in the Section S1 of the supplement). Figure 2c presents the minimum values of $\beta_{IA}C_{IA}/\sum\gamma$ for the studied clusters at lowest $C_{IA}$ ($10^6$ molecules cm$^{-3}$), where $\beta_{IA}$ is the rate coefficient of cluster collision with IA monomer, and $C_{IA}$ is the concentration of IA monomer. Figure 2d presents the results of the collision with MSA ($\beta_{MSA}C_{MSA}/\sum\gamma$). Similarly, the minimum values of $\beta_{IA}C_{IA}/\sum\gamma$ at 298 K and 258 K are presented in Fig. S2 and Fig. S3, respectively. Among these clusters, the largest (IA)$_4$·(MSA)$_2$ and (IA)$_6$ clusters ($\beta C/\sum\gamma$ >1) incline to collide with IA monomer (or MSA monomer) to grow out of the simulated system. As a result, the fluxes for clusters with larger size than (IA)$_4$·(MSA)$_2$ and (IA)$_6$ are counted in the cluster formation rate $J$.
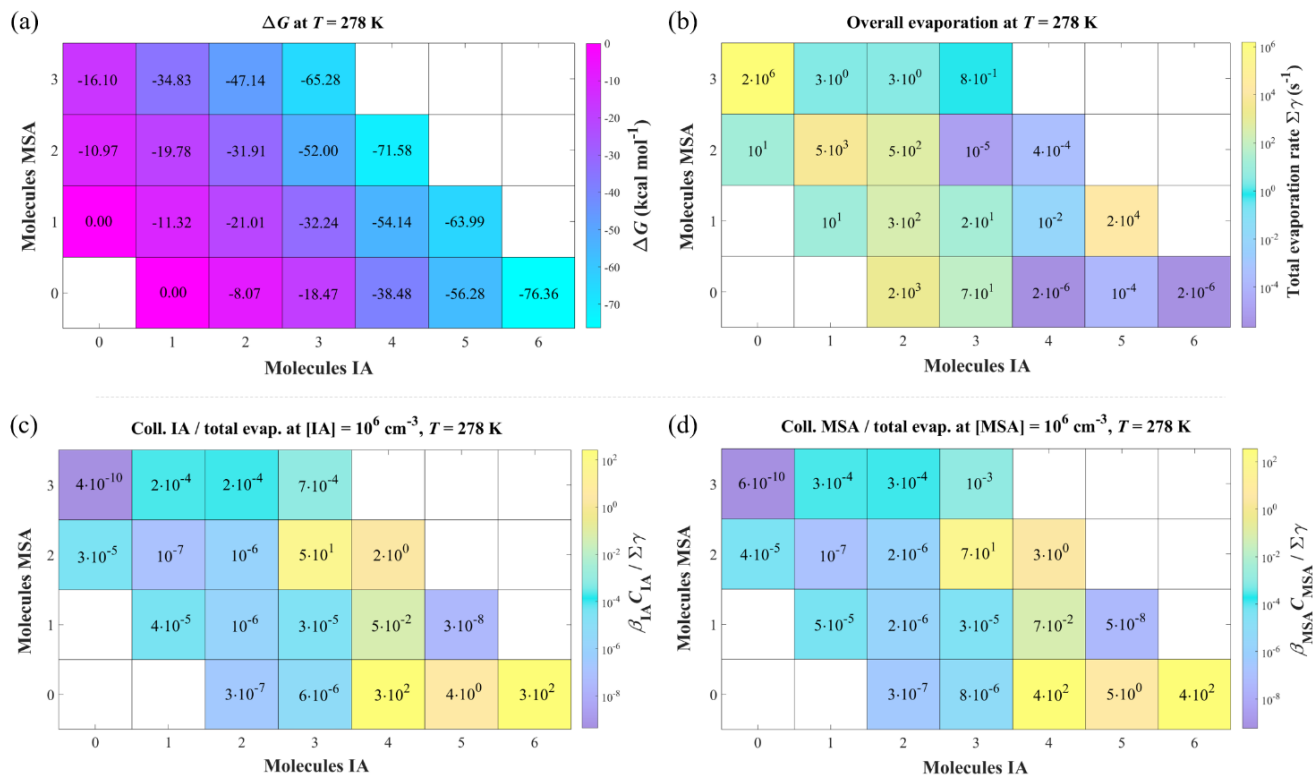
**Figure 2. (a)** Gibbs formation free energy ($\Delta G$, kcal mol$^{-1}$) of the (IA)$_x$(MSA)$_y$ ($0 \le x \le 6$, $0 \le y \le 3$, $1 < x + y \le 6$) clusters calculated at the RI-CC2/aug-cc-pV(T+d)Z(-PP)//$\omega$B97X-D/6-311++G(3df,3pd) + aug-cc-pVTZ-PP level of theory, $T = 278$ K, $p = 1$ atm. **(b)** the total evaporation rate coefficients ($\sum\gamma$, s$^{-1}$), and the ratios of collision frequencies with **(c)** IA monomer or **(d)** MSA monomer versus total evaporation rate coefficients ($\beta_{IA}C_{IA}/\sum\gamma$ or $\beta_{MSA}C_{MSA}/\sum\gamma$) of the corresponding clusters. $\beta$ is the rate coefficient of cluster collision with monomer, and $C$ is the monomer concentration.

### 3.3 Cluster formation rates

To comprehensively explore the effect of MSA on IA cluster formation kinetically, the IA-MSA cluster formation rate $J$ (cm$^{-3}$ s$^{-1}$) was simulated under different atmospheric conditions using ACDC. Herein, we first explored the changes of $J$ after the intervention of different concentrations of MSA ([MSA]), using the pure-IA system as a reference. Based on the field

measurement, [IA] in the ACDC simulation is set to be in the range of $10^6$–$10^8$ molecules cm$^{-3}$ (Sipila et al., 2016), [MSA] = $10^6$, $10^7$, and $10^8$ molecules cm$^{-3}$ (Chen et al., 2018; Berresheim et al., 2002; Davis et al., 1998). As to the setting of condensation sink coefficient (CS), the different CS ($1.0\times10^{-4}$ ~ $2.6\times10^{-3}$ s$^{-1}$) have an impact on the simulated $J$, especially in the case of low $J$ (Fig. S4), but less on presenting the promotion of MSA on IA cluster formation and the main conclusions of this study. Hence, the CS is chosen as a typical coastal value ($2.0 \times 10^{-3}$ s$^{-1}$) (Dal Maso et al., 2002), which is uniform for all clusters.
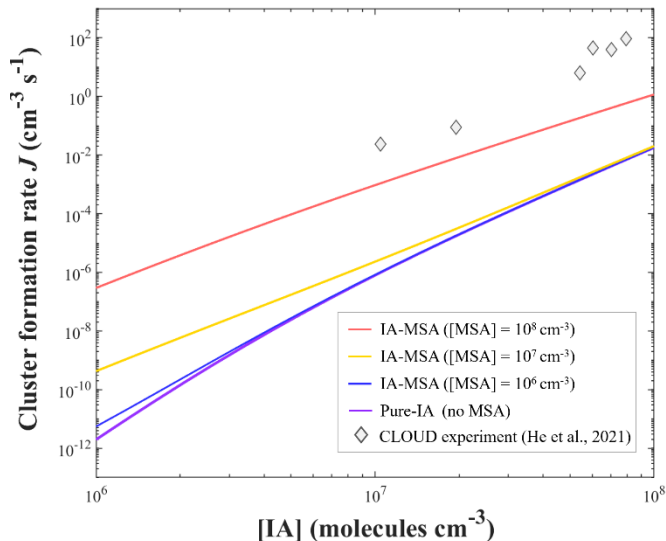
**Figure 3.** Simulated cluster formation rates $J$ (cm$^{-3}$ s$^{-1}$) as a function of iodic acid concentration [IA], with different concentrations of methanesulfonic acid [MSA] of $10^6$ (blue), $10^7$ (yellow), $10^8$ (red) and 0 molecules cm$^{-3}$ (purple, pure-IA), at $T = 278$ K, and CS = $2.0 \times 10^{-3}$ s$^{-1}$. The gray diamonds are the measured rate data from the CLOUD experiment at $T = 283$ K (He et al., 2021).

As shown in Fig. 3, the simulated $J$ of pure-IA nucleation (purple line) is much lower than the rate obtained from the CLOUD experiment (He et al. 2021). The $J$ of IA-MSA system with varying [MSA] (red, yellow, and blue lines) are all higher than that of the pure-IA system (purple line). Particularly, at a lower [IA] of $10^6$ molecules cm$^{-3}$, the involvement of MSA results in a greater boost on $J$. Briefly, MSA can promote $J$ of IA clusters to a higher level, which is a reflection of the stabilizing effect of MSA on IA clusters. However, the $J$ of IA-MSA nucleation was still much less than the experimental results (He et al. 2021), even at a high [MSA] ($10^8$ molecules cm$^{-3}$). The large rate difference suggests that MSA stabilizes IA less efficiently than the potential iodine-containing components.

To quantify such enhancement of the MSA on $J$, here we defined an enhancement strength $R$ as the following Eq. (5):

$$R = \frac{J_{\text{IA-MSA}}}{J_{\text{pure-IA}}} = \frac{J([\text{IA}] = x, [\text{MSA}] = y)}{J([\text{IA}] = x)} \tag{5}$$

where $J_{\text{IA-MSA}}$ and $J_{\text{pure-IA}}$ indicates the $J$ of IA-MSA and pure-IA nucleating system, respectively. $x$ and $y$ are the atmospheric concentrations of IA and MSA, respectively.

During nucleating processes, variations in ambient conditions (precursor concentration and temperature) can affect $J_{\text{IA-MSA}}$ and $J_{\text{pure-IA}}$ as well as the $R$ of MSA. Herein, the simulations were performed in a wide range of atmospheric temperatures ($T$ = 218 K − 298 K) and concentrations of IA ($10^6 − 10^8$ molecules cm$^{-3}$) and MSA ($10^6 − 10^8$ molecules cm$^{-3}$).
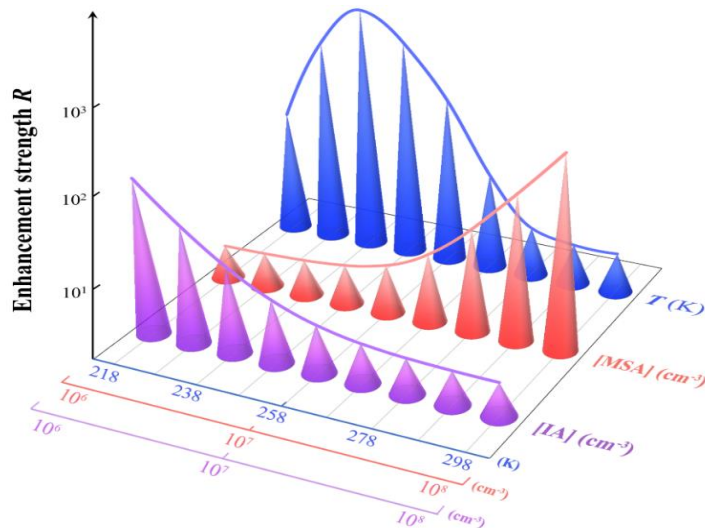
**Figure 4**. Enhancement strength $R$ of MSA on cluster formation rates under different atmospheric conditions: $T$ = 218 − 298 K (blue cones, [IA] = $10^7$ and [MSA] = $10^7$ molecules cm$^{-3}$), [MSA] = $10^6 − 10^8$ molecules cm$^{-3}$ (red cones, $T$ = 278 K and [IA] = $10^7$ molecules cm$^{-3}$), [IA] = $10^6 − 10^8$ molecules cm$^{-3}$ (purple cones, $T$ = 278 K and [MSA] = $10^7$ molecules cm$^{-3}$), and CS = $2.0 \times 10^{-3}$ s$^{-1}$.

As shown in Fig. 4, the enhancement strength $R$ of MSA decreases with the increasing of [IA] ($10^6 \rightarrow 10^8$ molecules cm$^{-3}$), under the condition of $T$ = 278 K and [MSA] = $10^7$ molecules cm$^{-3}$ (purple line). The specific $R$ values were summarized in Table S6. This is because the contribution of pure-IA clusters to nucleation becomes higher with the increasing of [IA], thereby diminishing that of IA-MSA clusters (smaller $R$). Conversely at lower [IA] ($10^6$ molecules cm$^{-3}$), the $R$ of MSA on $J$ could reach 211-fold, even when [MSA] is only at a median value ($10^7$ molecules cm$^{-3}$). The $R$ increases with the increasing of [MSA] ($10^6 \rightarrow 10^8$ molecules cm$^{-3}$) (orange line) due to more IA-MSA clusters formed. Interestingly, as the temperature decreases from 298 K to 218 K (blue line), $R$ first increases (298 K $\rightarrow$ 238 K) and then decreases (238 K $\rightarrow$ 218 K). During the temperatures range from 298 K to 238 K, the decrease in temperature diminishes cluster evaporation (Eq. (4)), which in turn promotes IA-MSA cluster formation and leads to an increase in $R$. When the temperature is very low, between 218 and 238 K, the effect of cluster evaporation is almost negligible, and the nucleation process is primarily limited by collisions between clusters or molecules, namely the kinetic limit process. In this case, the lower $T$ reduces the collision rate and thus results in a decrease in $R$. Because the numerator $J_{\text{IA-MSA}}$ in Eq. (5) is affected by the formation of both pure-IA clusters and IA-MSA

clusters, while the denominator $J_{pure\text{-}IA}$ is only affected by the formation of pure-IA clusters. When the overall intermolecular collision rate between IA and IA, as well as IA and MSA, is reduced due to the decrease in temperature, the numerator would be affected more than the denominator in Eq. (5), which in turn leads to a reduced $R$. As a result of the above analysis, the effect of the IA-MSA system on the nucleation process varies with the [IA], [MSA] and $T$, and is particularly important in regions with lower $T$, sparse IA, and rich MSA.

### 3.4 Cluster growth pathways

According to the analysis above, MSA can stabilize IA clusters, thereby enhancing cluster formation rate. However, the mechanism of how MSA and IA jointly contribute to cluster formation is still unclear. Thus, the detailed cluster growth pathways were tracked by ACDC and shown in Fig. 5a.
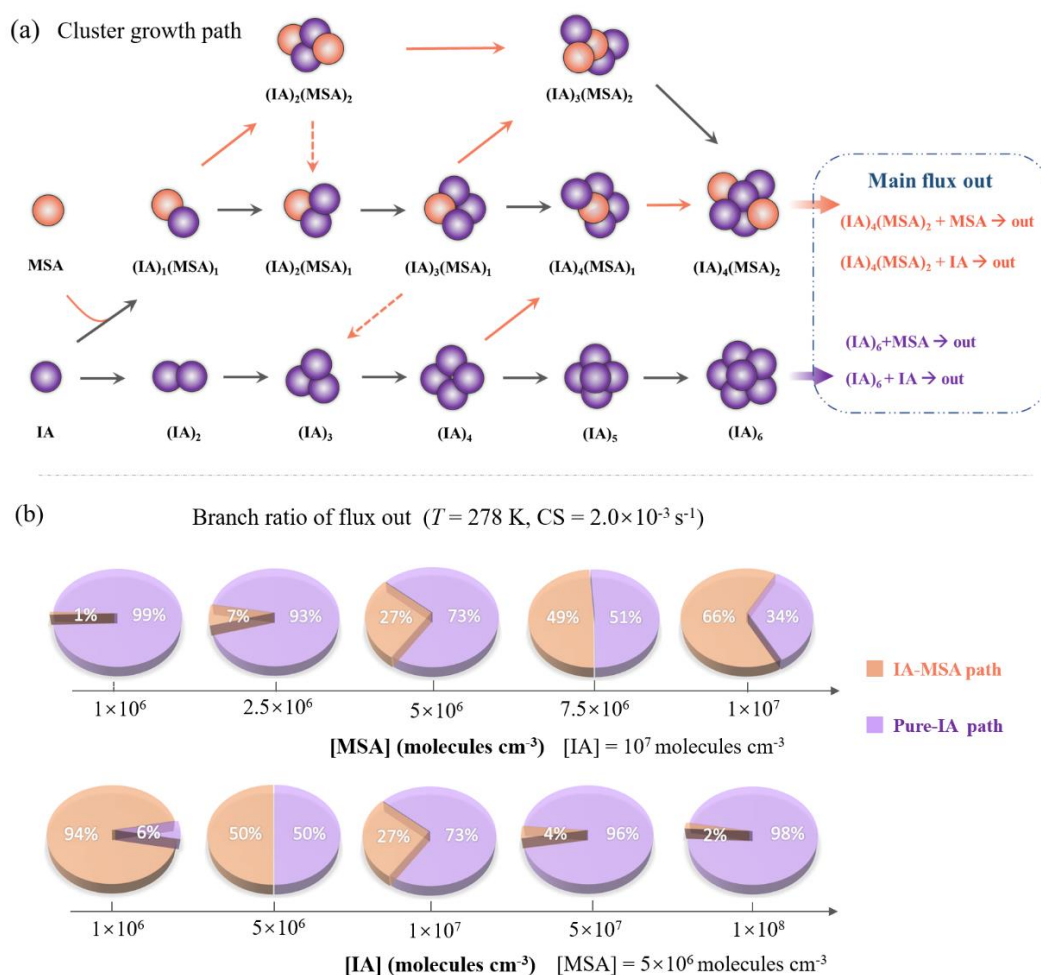
**Figure 5. (a)** Main cluster growth pathway of IA-MSA nucleating system at $T = 278$ K, CS $= 2.0\times10^{-3}$ s$^{-1}$, [IA] $= 10^7$ and [MSA] $= 5\times10^6$ molecules cm$^{-3}$. The black and orange arrows refer to the pathways of colliding with IA and MSA,

respectively, where the dashed arrows indicate the evaporation of MSA. **(b)** Branch ratio of IA-MSA (orange pie) and pure-IA (purple pie) growth pathway under varying [MSA] ($10^6 - 10^7$ molecules cm$^{-3}$) and [IA] ($10^6 - 10^8$ molecules cm$^{-3}$).

The main clustering pathways can be divided into two types: i) IA self-nucleation and ii) IA-MSA cluster formation. The studied clusters that did not appear in the cluster growth pathway are mainly due to their low stability. For the IA self-nucleation pathway, cluster growth proceeds mainly via the collisional binding of IA monomers ($(IA)_{1\to2\to3\to4\to5\to6}$), which is consistent with the reported pure-IA nucleation mechanism (Rong et al., 2020). For the IA-MSA pathway, it starts from the heterodimer $(IA)_1 \cdot (MSA)_1$, and then grows primarily through IA addition, resulting in the $(IA)_4 \cdot (MSA)_2$ clusters with sufficient stability to grow out of the simulated system (Fig. 2c). The results suggest that MSA can directly participate in the IA-involved nucleation by forming relatively stable IA-MSA clusters.

In the atmosphere, the distribution of IA and MSA varies by regions, affecting the contribution of IA-MSA clustering pathways accordingly. Hence, the branch ratios of flux out through the IA-MSA path (orange pie) and pure-IA path (purple pie) at varying [MSA] ($10^6 - 10^7$ molecules cm$^{-3}$) and [IA] ($10^6 - 10^8$ molecules cm$^{-3}$) are presented in Fig. 5b to access the impact of IA-MSA mechanism. As shown in Fig. 5b, the branch ratio of IA-MSA and pure-IA path is highly dependent on [MSA] and [IA]. At the condition of $T = 278$ K, CS $= 2.0 \times 10^{-3}$ s$^{-1}$ and [IA] $= 10^7$ molecules cm$^{-3}$, the contribution of IA-MSA path increases from 1% to 66% with the increasing of [MSA]. Additionally, given the uneven distribution of IA, the analysis was further carried out within the atmospherically relevant range of [IA] ($10^6 - 10^8$ molecules cm$^{-3}$). The results show that the contribution of IA-MSA path decreases from 94% to 2% with the increasing of [IA] ($10^6 - 10^8$ molecules cm$^{-3}$). These findings indicate that the IA-MSA mechanism contributes more in regions with higher [MSA] and lower [IA]. Furthermore, the branch ratio was calculated based on field conditions (temperatures and [IA]) reported by He et al., (2021) and presented in Fig. S5. The results indicate that the IA-MSA mechanism does have stronger effects in polar regions than in mid-latitude coastal regions due to lower temperatures, which is also consistent with the above findings.

Most of the analysis above in the text was performed at 278 K. To further probe the impact of temperature on $J$ systematically, Figure. 6 presents the simulated $J$ at additional temperatures (218, 238, 258 and 298 K), [IA] $= 10^6 - 10^8$ molecules cm$^{-3}$, [MSA] $= 10^6$ (red line), $10^7$ (yellow line), and $10^8$ molecules cm$^{-3}$ (purple line). At a relatively high $T = 298$ K (Fig. 6d), the improvement on $J$ by the addition of MSA was not significant compared to the pure-IA system, except at higher [MSA] $= 10^8$ molecules cm$^{-3}$ and relatively lower [IA]. At lower $T = 258$ K (Fig. 6c), the enhancement on $J$ by MSA is stronger in all cases except at lowest [MSA] $= 10^6$ molecules cm$^{-3}$. Moreover, such boost on $J$ was further enhanced at 238 K (Fig. 6b). Lower concentrations of MSA ($10^6$ molecules cm$^{-3}$) also significantly promote the formation of IA clusters, mainly because the low temperature weakens the cluster evaporation.
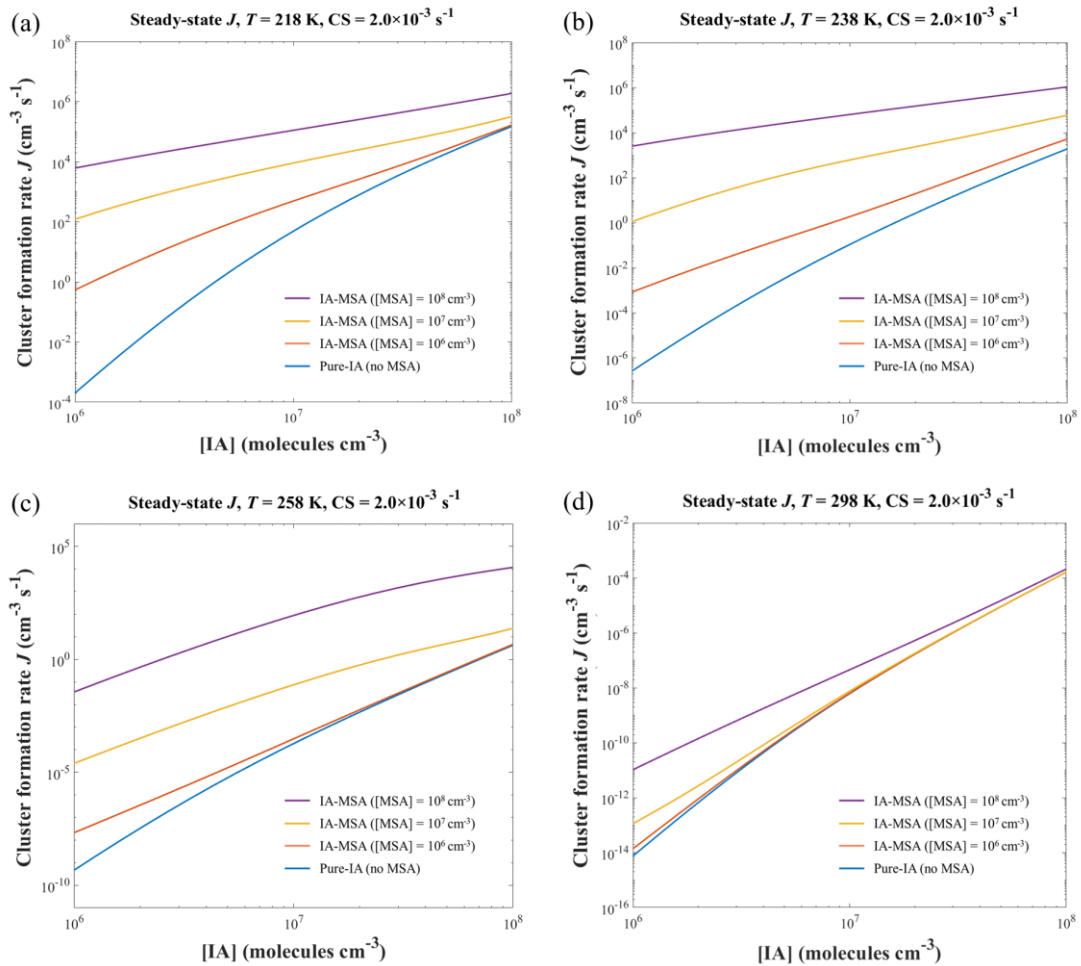
**Figure 6**. The simulated cluster formation rate $J$ (cm$^{-3}$ s$^{-1}$) of the IA-MSA system at different temperatures (a) 218, (b) 238, (c) 258, (d) 298 K, [IA] = $10^6$ – $10^8$ molecules cm$^{-3}$, [MSA] = 0, $10^6$, $10^7$, $10^8$ molecules cm$^{-3}$, and CS = $2.0 \times 10^{-3}$ s$^{-1}$.

Interestingly, the comparison of the simulations at 218 K (Fig. 6a) and 238 K (Fig. 6b) shows that the decrease in temperature does not further improve $J$ to a higher level. Instead, there is a decrease of the enhancement of MSA at higher [IA] = $10^7$–$10^8$ molecules cm$^{-3}$. The reason for this phenomenon, which was also discussed in Section 3.3, is that at such low temperatures, cluster growth is more dependent on collisions and less on evaporation. And the low temperature reduces the rate of collision between clusters or molecules.

Compared to the field observations at Mace Head (Sipila et al. 2016) and Arctic Sites (Beck et al. 2021) The rate of the IA-MSA mechanism is also significantly lower. This indicates that the contribution of MSA to IA particle formation under atmospheric conditions is relatively limited, and more efficient stabilizer for IA should be involved in the nucleating process, such as other iodine-containing components such as HIO$_2$ and iodine oxides (I$_2$O$_4$ and I$_2$O$_5$). Moreover, considering the

complexity of the marine atmosphere, other non-iodine nucleation precursors, such as SA, NH$_3$, amines, etc., may also affect the nucleation process. Particularly with SA, because MSA and SA coexist in the air and both are formed during the oxidation of DMS in the marine atmosphere. Therefore, in future studies, the influence of the above factors on the nucleation mechanism of marine aerosols will also be considered.

## 4 Atmospheric significance and conclusion

The present work systematically investigates the joint nucleation mechanisms of two critical marine nucleation precursors, methanesulfonic acid (MSA) and iodic acid (IA), using the quantum chemical approach and Atmospheric Cluster Dynamics Code (ACDC). The results suggest that the self-nucleation rate of IA is much lower than that of CLOUD experiment, indicating the importance of stabilizers for IA in the nucleation process. We find that MSA can stabilize IA cluster via both hydrogen and halogen bonds, and thus promote IA cluster formation rate, especially in low-temperature environments with sparse IA and rich MSA. The corresponding IA-MSA nucleating mechanism can be described by two distinct pathways: i) pure-IA cluster formation and ii) IA-MSA cluster formation, indicating that IA and MSA can jointly nucleate. The IA-MSA nucleation is highly dependent on the distribution of MSA and IA in the marine atmosphere. However, IA-MSA nucleation rates are far from sufficient to explain the field observations, indicating that additional essential precursors need to be considered (e.g., H$_2$SO$_4$, HIO$_2$, NH$_3$ and amines). Nucleation among these components is likely to be synergistic, with only varying magnitudes of contribution. For example, both SA and MSA originate from the oxidation of DMS, so their coexistence in the atmosphere may synergistically promote the formation of IA clusters, which is worthy of future studies.

The current study provides molecular-level evidence that IA and MSA can jointly nucleate and the IA-MSA joint nucleation is more efficient than the IA self-nucleation. More broadly, this finding helps to construct a more comprehensive marine multi-component nucleation model.

*Competing interests*. The authors declare that they have no conflict of interest.

*Data availability*. The data in this article are available from the corresponding author upon request (zhangxiuhui@bit.edu.cn)

*Author contributions*. AN: Data curation, Formal analysis, Investigation, Visualization, Writing – original draft preparation; LL: Validation, Visualization. LJ: Validation, Writing review & editing. XHZ: Supervision, Conceptualization, Writing - review & editing, Formal analysis, Data curation.

*Acknowledgements*. We acknowledge the National Supercomputing Centre in Shenzhen for providing the computational resources and Turbomole program.

*Financial support*. This work was supported by the National Natural Science Foundation of China (21976015). L. L. thanks the China Postdoctoral Science Foundation (2020M680013) and the National Natural Science Foundation of China (4210050126).

## References

Ahlrichs, R., Bär, M., Häser, M., Horn, H., & Kölmel, C.: Electronic-Structure Calculations on Workstation Computers: The program system turbomole, Chem. Phys. Lett., 162(3), 165-169, https://doi.org/10.1016/0009-2614(89)85118-8, 1989.

Almeida, J., Schobesberger, S., Kürten, A., Ortega, I. K., Kupiainen-Määttä, O., Praplan, A. P., Adamov, A., Amorim, A., Bianchi, F., Breitenlechner, M., David, A., Dommen, J., Donahue, N. M., Downard, A., Dunne, E., Duplissy, J., Ehrhart, S., Flagan, R. C., Franchin, A., Guida, R., Hakala, J., Hansel, A., Heinritzi, M., Henschel, H., Jokinen, T., Junninen, H., Kajos, M., Kangasluoma, J., Keskinen, H., Kupc, A., Kurtén, T., Kvashin, A. N., Laaksonen, A., Lehtipalo, K., Leiminger, M., Leppä, J., Loukonen, V., Makhmutov, V., Mathot, S., McGrath, M. J., Nieminen, T., Olenius, T., Onnela, A., Petäjä, T., Riccobono, F., Riipinen, I., Rissanen, M., Rondo, L., Ruuskanen, T., Santos, F. D., Sarnela, N., Schallhart, S., Schnitzhofer, R., Seinfeld, J. H., Simon, M., Sipilä, M., Stozhkov, Y., Stratmann, F., Tomé, A., Tröstl, J., Tsagkogeorgas, G., Vaattovaara, P., Viisanen, Y., Virtanen, A., Vrtala, A., Wagner, P. E., Weingartner, E., Wex, H., Williamson, C., Wimmer, D., Ye, P., Yli-Juuti, T., Carslaw, K. S., Kulmala, M., Curtius, J., Baltensperger, U., Worsnop, D. R., Vehkamäki, H., and Kirkby, J.: Molecular understanding of sulphuric acid–amine particle nucleation in the atmosphere, Nature, 502, 359–363, https://doi.org/10.1038/nature12663, 2013.

Arquero, K. D., Xu, J., Gerber, R. B., & Finlayson-Pitts, B. J.: Particle formation and growth from oxalic acid, methanesulfonic acid, trimethylamine and water: a combined experimental and theoretical study. Phys. Chem. Chem. Phys, 19(41), 28286-28301, https://doi.org/10.1039/C7CP04468B, 2017.

Baccarini, A., Karlsson, L., Dommen, J., Duplessis, P., Vüllers, J., Brooks, I. M., Saiz-Lopez, A., Salter, M., Tjernström, M., Baltensperger, U., Zieger, P., and Schmale, J.: Frequent new particle formation over the high Arctic pack ice by enhanced iodine emissions, Nat. Commun., 11, 4924, https://doi.org/10.1038/s41467-020-18551-0, 2020.

Bates, T. S., Lamb, B. K., Guenther, A., Dignon, J., and Stoiber, R. E.: Sulfur emissions to the atmosphere from natural sources. J. Atmos. Chem., 14(1-4), 315-337, https://doi.org/10.1007/BF00115242,1992.

Beck, L. J., Sarnela, N., Junninen, H., Hoppe, C. J. M., Garmash, O., Bianchi, F., Riva, M., Rose, C., Peräkylä, O., Wimmer, D., Kausiala, O., Jokinen, T., Ahonen, L., Mikkilä, J., Hakala, J., He, X., Kontkanen, J., Wolf, K. K. E., Cappelletti, D., Mazzola, M., Traversi, R., Petroselli, C., Viola, A. P., Vitale, V., Lange, R., Massling, A., Nøjgaard, J. K., Krejci, R., Karlsson, L., Zieger, P., Jang, S., Lee, K., Vakkari, V., Lampilahti, J., Thakur, R. C., Leino, K., Kangasluoma, J., Duplissy, E., Siivola, E., Marbouti, M., Tham, Y. J., Saiz-Lopez, A., Petäjä, T., Ehn, M., Worsnop, D. R., Skov, H., Kulmala, M., Kerminen, V., and Sipilä, M.: Differing Mechanisms of New Particle Formation at Two Arctic Sites, Geophys. Res. Lett., 48, https://doi.org/10.1029/2020GL091334, 2021.

Becke, A.: The quantum theory of atoms in molecules: from solid state to DNA and drug design, John Wiley & Sons, 2007.

Berresheim, H., Elste, T., Tremmel, H. G., Allen, A. G., Hansson, H. C., Rosman, K., Dal Maso, M., Makela, J. M., Kulmala, M., and O'Dowd, C. D.: Gas-aerosol relationships of $H_2SO_4$, MSA, and OH: Observations in the coastal marine boundary layer at Mace Head, Ireland, J. Geophys. Res.: Atmos., 107, https://doi.org/10.1029/2000jd000229, 2002.

Charlson, R. J., Lovelock, J. E., Andreae, M. O., and Warren, S. G.: Oceanic Phytoplankton, Atmospheric Sulfur, Cloud Albedo and Climate, Nature, 326, 655-661, https://doi.org/10.1038/326655a0, 1987.

Chen, Q., Sherwen, T., Evans, M., and Alexander, B.: DMS oxidation and sulfur aerosol formation in the marine troposphere: a focus on reactive halogen and multiphase chemistry, Atmos. Chem. Phys., 18, 13617–13637, https://doi.org/10.5194/acp-18-13617-2018, 2018.

Dal Maso, M., Kulmala, M., Lehtinen, K. E. J., Makela, J. M., Aalto, P., and O'Dowd, C. D.: Condensation and coagulation sinks and formation of nucleation mode particles in coastal and boreal forest boundary layers, J. Geophys. Res.: Atmos., 107(D19), PAR-2, https://doi.org/10.1029/2001jd001053, 2002.

Davis, D., Chen, G., Kasibhatla, P., Jefferson, A., Tanner, D., Eisele, F., Lenschow, D., Neff, W., and Berresheim, H.: DMS oxidation in the Antarctic marine boundary layer: Comparison of model simulations and field observations of DMS, DMSO, $DMSO_2$, $H_2SO_4(g)$, MSA(g), and MSA(p), J. Geophys. Res.: Atmos., 103, 1657-1678, https://doi.org/10.1029/97jd03452, 1998.

Dawson, M. L., Varner, M. E., Perraud, V., Ezell, M. J., Gerber, R. B., and Finlayson-Pitts, B. J.: Simplified mechanism for new particle formation from methanesulfonic acid, amines, and water via experiments and ab initio calculations, Proc. Natl. Acad. Sci. U. S. A., 109, 18719-18724, https://doi.org/10.1073/pnas.1211878109, 2012.

Dunning, T. H., Peterson, K. A., and Wilson, A. K.: Gaussian basis sets for use in correlated molecular calculations. X. The atoms aluminum through argon revisited, J. Chem. Phys., 114, 9244-9253, https://doi.org/10.1063/1.1367373, 2001.

Eisele, F. L. and Tanner, D. J.: Measurement of the gas phase concentration of $H_2SO_4$ and methane sulfonic acid and estimates of $H_2SO_4$ production and loss in the atmosphere, J. Geophys. Res.: Atmos., 98, 9001-9010, https://doi.org/10.1029/93JD00031, 1993.

Elm, J. and Kristensen, K.: Basis set convergence of the binding energies of strongly hydrogen-bonded atmospheric clusters, Phys. Chem. Chem. Phys., 19, 1122–1133, https://doi.org/10.1039/C6CP06851K, 2017.

Francl, M. M., Pietro, W. J., Hehre, W. J., Binkley, J. S., Gordon, M. S., DeFrees, D. J., and Pople, J. A.: Self-consistent molecular orbital methods. XXIII. A polarization-type basis set for second-row elements, J. Chem. Phys., 77, 3654-3665, https://doi.org/10.1063/1.444267, 1982.

Frisch, M. J., Trucks, G. W., Schlegel, H. B., Scuseria, G. E., and M. A. Robb, J. R. C., G. Scalmani, V. Barone, G. A. Petersson, H. Nakatsuji, X. Li, M. Caricato, A. Marenich, J. Bloino, B. G. Janesko, R. Gomperts, B. Mennucci, H. P. Hratchian, J. V. Ortiz, A. F. Izmaylov, J. L. Sonnenberg, D. Williams-Young, F. Ding, F. Lipparini, F. Egidi, J. Goings, B. Peng, A. Petrone, T. Henderson, D. Ranasinghe, V. G. Zakrzewski, J. Gao, N. Rega, G. Zheng, W. Liang, M. Hada, M. Ehara, K. Toyota, R. Fukuda, J. Hasegawa, M. Ishida, T. Nakajima, Y. Honda, O. Kitao, H. Nakai, T. Vreven, K. Throssell, J. A. Montgomery, Jr., J. E. Peralta, F. Ogliaro, M. Bearpark, J. J. Heyd, E. Brothers, K. N. Kudin, V. N. Staroverov, T. Keith, R. Kobayashi, J. Normand, K. Raghavachari, A. Rendell, J. C. Burant, S. S. Iyengar, J. Tomasi, M. Cossi, J. M. Millam, M. Klene, C. Adamo, R. Cammi, J. W. Ochterski, R. L. Martin, K. Morokuma, O. Farkas, J. B. Foresman, and D. J. Fox: Gaussian 09, Revision A.02; Gaussian, Inc.: Wallingford, CT, 2009.

375    Grabowski, S. J.: Hydrogen bonding strength—measures based on geometric and topological parameters, J. Phys. Org. Chem., 17, 18-31, https://doi.org/10.1002/poc.685, 2004.

Hatakeyama, S., Okuda, M., and Akimoto, H.: Formation of sulfur dioxide and methanesulfonic acid in the photooxidation of dimethyl sulfide in the air, Geophys. Res. Lett., 9, 583-586, https://doi.org/10.1029/GL009i005p00583, 1982.

Hattig, C. and Weigend, F.: CC2 excitation energy calculations on large molecules using the resolution of the identity
380    approximation, J. Chem. Phys., 113, 5154-5161, https://doi.org/10.1063/1.1290013, 2000.

He, X.-C., Tham, Y. J., Dada, L., Wang, M., Finkenzeller, H., Stolzenburg, D., Iyer, S., Simon, M., Kürten, A., Shen, J., Rörup, B., Rissanen, M., Schobesberger, S., Baalbaki, R., Wang, D. S., Koenig, T. K., Jokinen, T., Sarnela, N., Beck, L. J., Almeida, J., Amanatidis, S., Amorim, A., Ataei, F., Baccarini, A., Bertozzi, B., Bianchi, F., Brilke, S., Caudillo, L., Chen, D., Chiu, R., Chu, B., Dias, A., Ding, A., Dommen, J., Duplissy, J., El Haddad, I., Gonzalez Carracedo, L., Granzin, M., Hansel, A., Heinritzi,
385    M., Hofbauer, V., Junninen, H., Kangasluoma, J., Kemppainen, D., Kim, C., Kong, W., Krechmer, J. E., Kvashin, A., Laitinen, T., Lamkaddam, H., Lee, C. P., Lehtipalo, K., Leiminger, M., Li, Z., Makhmutov, V., Manninen, H. E., Marie, G., Marten, R., Mathot, S., Mauldin, R. L., Mentler, B., Möhler, O., Müller, T., Nie, W., Onnela, A., Petäjä, T., Pfeifer, J., Philippov, M., Ranjithkumar, A., Saiz-Lopez, A., Salma, I., Scholz, W., Schuchmann, S., Schulze, B., Steiner, G., Stozhkov, Y., Tauber, C., Tomé, A., Thakur, R. C., Väisänen, O., Vazquez-Pufleau, M., Wagner, A. C., Wang, Y., Weber, S. K., Winkler, P. M., Wu,
390    Y., Xiao, M., Yan, C., Ye, Q., Ylisirniö, A., Zauner-Wieczorek, M., Zha, Q., Zhou, P., Flagan, R. C., Curtius, J., Baltensperger, U., Kulmala, M., Kerminen, V.-M., Kurtén, T., et al.: Role of iodine oxoacids in atmospheric aerosol nucleation, Science, 371, 589–595, https://doi.org/10.1126/science.abe0298, 2021.

Hodshire, A. L., Campuzano-Jost, P., Kodros, J. K., Croft, B., Nault, B. A., Schroder, J. C., Jimenez, J. L., and Pierce, J. R.: The potential role of methanesulfonic acid (MSA) in aerosol formation and growth and the associated radiative forcings, Atmos.
395    Chem. Phys., 19, 3137-3160, https://doi.org/10.5194/acp-19-3137-2019, 2019.

Humphrey, W., Dalke, A., and Schulten, K.: VMD: Visual molecular dynamics, J.    Mol.    Graphics,    14,    33–38, https://doi.org/10.1016/0263-7855(96)00018-5, 1996.

IPCC: Long-term climate change: projections, commitments and irreversibility, in: Climate Change 2013-The Physical Science Basis: Contribution of Working Group I to the Fifth Assessment Report of the Intergovernmental Panel on Climate
400    Change, Cambridge University Press, 1029-1136, 2013.

Karl, M., Gross, A., Leck, C., and Pirjola, L.: Intercomparison of dimethylsulfide oxidation mechanisms for the marine boundary layer: Gaseous and particulate sulfur constituents, J. Geophys. Res.: Atmos., 112, D15304, https://doi.org/10.1029/2006jd007914, 2007.

Kerminen, V.-M., Chen, X., Vakkari, V., Petäjä, T., Kulmala, M., and Bianchi, F.: Atmospheric new particle formation and
405    growth: review of field observations, Environ. Res. Lett., 13, 103003, https://doi.org/10.1088/1748-9326/aadf3c, 2018.

Khanniche, S., Louis, F., Cantrel, L., & Černušák, I.: A theoretical study of the microhydration of iodic acid (HOIO2). Comput. Theor. Chem., 1094, 98-107, https://doi.org/10.1016/j.comptc.2016.09.010, 2016.

Koch, U. and Popelier, P. L. A.: Characterization of CHO hydrogen bonds on the basis of the charge density, J. Phys. Chem., 99, 9747-9754, https://doi.org/10.1021/j100024a016, 1995.

410   Kulmala, M.: How particles nucleate and grow, Science, 302, 1000-1001, https://doi.org/10.1126/science.1090848, 2003.

Kulmala, M., Kontkanen, J., Junninen, H., Lehtipalo, K., Manninen, H. E., Nieminen, T., Petäjä, T., Sipilä, M., Schobesberger, S., Rantala, P., Franchin, A., Jokinen, T., Järvinen, E., Äijälä, M., Kangasluoma, J., Hakala, J., Aalto, P. P., Paasonen, P., Mikkilä, J., Vanhanen, J., Aalto, J., Hakola, H., Makkonen, U., Ruuskanen, T., Mauldin, R. L., III, Duplissy, J., Vehkamäki, H., Bäck, J., Kortelainen, A., Riipinen, I., Kurtén, T., Johnston, M. V., Smith, J. N., Ehn, M., Mentel, T. F., Lehtinen, K. E. J.,

415   Laaksonen, A., Kerminen, V.-M., and Worsnop, D. R.: Direct Observations of Atmospheric Aerosol Nucleation, Science, 339, 943-946, https://doi.org/10.1126/science.1227385, 2013.

Kürten, A., Li, C., Bianchi, F., Curtius, J., Dias, A., Donahue, N. M., Duplissy, J., Flagan, R. C., Hakala, J., Jokinen, T., Kirkby, J., Kulmala, M., Laaksonen, A., Lehtipalo, K., Makhmutov, V., Onnela, A., Rissanen, M. P., Simon, M., Sipilä, M., Stozhkov, Y., Tröstl, J., Ye, P., and McMurry, P. H.: New particle formation in the sulfuric acid–dimethylamine–water system:

420   reevaluation of CLOUD chamber measurements and comparison to an aerosol nucleation and growth model, Atmos. Chem. Phys., 18, 845-863, https://doi.org/10.5194/acp-18-845-2018, 2018.

Lane, J. R., Contreras-García, J., Piquemal, J.-P., Miller, B. J., and Kjaergaard, H. G.: Are bond critical points really critical for hydrogen bonding?, Journal of Chemical Theory and Computation, 9, 3263-3266, https://doi.org/10.1021/ct400420r, 2013.

Li, H., Ning, A., Zhong, J., Zhang, H., Liu, L., Zhang, Y., Zhang, X., Zeng, X. C., and He, H.: Influence of atmospheric

425   conditions on sulfuric acid-dimethylamine-ammonia-based new particle formation, Chemosphere, 245, 125554, https://doi.org/10.1016/j.chemosphere.2019.125554, 2020.

Lu, T. and Chen, F. W.: Multiwfn: A multifunctional wavefunction analyzer, J. Comput. Chem., 33, 580-592, https://doi.org/10.1002/jcc.22885, 2012.

Lu, T. and Chen, Q.: Shermo: A general code for calculating molecular thermochemistry properties, Comput. Theor. Chem.,

430   1200, 113249, https://doi.org/10.1016/j.comptc.2021.113249, 2021.

Lu, Y., Liu, L., Ning, A., Yang, G., Liu, Y., Kurtén, T., Vehkamäki, H., Zhang, X., and Wang, L.: Atmospheric sulfuric acid-dimethylamine nucleation enhanced by trifluoroacetic acid, Geophys. Res. Lett., 47, e2019GL085627, https://doi.org/10.1029/2019GL085627, 2020.

MacKerell, A. D., Bashford, D., Bellott, M., Dunbrack, R. L., Evanseck, J. D., Field, M. J., Fischer, S., Gao, J., Guo, H., Ha,

435   S., Joseph-McCarthy, D., Kuchnir, L., Kuczera, K., Lau, F. T. K., Mattos, C., Michnick, S., Ngo, T., Nguyen, D. T., Prodhom, B., Reiher, W. E., Roux, B., Schlenkrich, M., Smith, J. C., Stote, R., Straub, J., Watanabe, M., Wiórkiewicz-Kuczera, J., Yin, D., and Karplus, M.: All-Atom Empirical Potential for Molecular Modeling and Dynamics Studies of Proteins, J. Phys. Chem. B, 102, 3586-3616, https://doi.org/10.1021/jp973084f, 1998.

Martín, J. C. G., Lewis, T. R., Blitz, M. A., Plane, J. M., Kumar, M., Francisco, J. S., and Saiz-Lopez, A.: A gas-to-particle

440   conversion mechanism helps to explain atmospheric particle formation through clustering of iodine oxides, Nat. Commun., 11, 4521, https://doi.org/10.1038/s41467-020-18252-8, 2020.

McGrath, M. J., Olenius, T., Ortega, I. K., Loukonen, V., Paasonen, P., Kurtén, T., Kulmala, M., and Vehkamäki, H.: Atmospheric Cluster Dynamics Code: a flexible method for solution of the birth-death equations, Atmos. Chem. Phys., 12, 2345-2355, https://doi.org/10.5194/acp-12-2345-2012, 2012.

445   Merikanto, J., Spracklen, D., Mann, G., Pickering, S., and Carslaw, K.: Impact of nucleation on global CCN, Atmos. Chem. Phys., 9, 8601-8616, https://doi.org/10.5194/acp-9-8601-2009, 2009.

Ning, A., Zhang, H., Zhang, X., Li, Z., Zhang, Y., Xu, Y., and Ge, M.: A molecular-scale study on the role of methanesulfinic acid in marine new particle formation, Atmos. Environ., 227, 117378, https://doi.org/10.1016/j.atmosenv.2020.117378, 2020.

O'Dowd, C. D. and de Leeuw, G.: Marine aerosol production: a review of the current knowledge, Philos. Trans. R. Soc., A, 450   365, 1753-1774, https://doi.org/10.1098/rsta.2007.2043, 2007.

O'Dowd, C. D., Jimenez, J. L., Bahreini, R., Flagan, R. C., Seinfeld, J. H., Hämeri, K., Pirjola, L., Kulmala, M., Jennings, S. G., and Hoffmann, T.: Marine aerosol formation from biogenic iodine emissions, Nature, 417, 632–636, https://doi.org/10.1038/nature00775, 2002.

Perraud, V., Horne, J. R., Martinez, A. S., Kalinowski, J., Meinardi, S., Dawson, M. L., Wingen, L. M., Dabdub, D., Blake, D. 455   R., Gerber, R. B., and Finlayson-Pitts, B. J.: The future of airborne sulfur-containing particles in the absence of fossil fuel sulfur dioxide emissions, Proc. Natl. Acad. Sci. U. S. A., 112, 13514–13519, https://doi.org/10.1073/pnas.1510743112, 2015.

Peterson, K. A., Figgen, D., Goll, E., Stoll, H., and Dolg, M.: Systematically convergent basis sets with relativistic pseudopotentials. II. Small-core pseudopotentials and correlation consistent basis sets for the post-d group 16–18 elements, J. Chem. Phys., 119, 11113-11123, https://doi.org/10.1063/1.1622924, 2003.

460   Reed, A. E., Curtiss, L. A., and Weinhold, F.: Intermolecular interactions from a natural bond orbital, donor-acceptor viewpoint, Chem. Rev., 88, 899-926, https://doi.org/10.1021/cr00088a005, 1988.

Rong, H., Liu, J., Zhang, Y., Du, L., Zhang, X., and Li, Z.: Nucleation mechanisms of iodic acid in clean and polluted coastal regions, Chemosphere, 253, 126743, https://doi.org/10.1016/j.chemosphere.2020.126743, 2020.

Rozas, I., Alkorta, I., and Elguero, J.: Behavior of ylides containing N, O, and C atoms as hydrogen bond acceptors, J. Am. 465   Chem. Soc., 122, 11154-11161, https://doi.org/10.1021/ja0017864, 2000.

Rappé, A. K., Casewit, C. J., Colwell, K. S., Goddard III, W. A., & Skiff, W. M.: UFF, a full periodic table force field for molecular mechanics and molecular dynamics simulations
. J. Am. Chem. Soc., 114(25), 10024-10035, https://doi.org/10.1021/ja00051a040, 1992.

Schmitz, G. and Elm, J.: Assessment of the DLPNO Binding Energies of Strongly Noncovalent Bonded Atmospheric 470   Molecular Clusters, ACS omega, 5, 7601-7612, https://doi.org/10.1021/acsomega.0c00436, 2020.

Shaw, G. E.: Bio-Controlled Thermostasis Involving the Sulfur Cycle, Clim. Change, 5, 297-303, https://doi.org/10.1007/Bf02423524, 1983.

Sipilä, M., Sarnela, N., Jokinen, T., Henschel, H., Junninen, H., Kontkanen, J., Richters, S., Kangasluoma, J., Franchin, A., Peräkylä, O., Rissanen, M. P., Ehn, M., Vehkamäki, H., Kurten, T., Berndt, T., Petäjä, T., Worsnop, D., Ceburnis, D., Kerminen,

475    V.-M., Kulmala, M., and O'Dowd, C.: Molecular-scale evidence of aerosol particle formation via sequential addition of HIO3, Nature, 537, 532-534, https://doi.org/10.1038/nature19314, 2016.

Stewart, J. J. P.: Optimization of parameters for semiempirical methods VI: more modifications to the NDDO approximations and re-optimization of parameters, J. Mol. Model., 19, 1-32, https://doi.org/10.1007/s00894-012-1667-x, 2013.

Stewart, J. J. P.: MOPAC2016, Colorado Springs,CO(USA), http://openmopac.net/MOPAC2016.html, 2016.

480    Takegawa, N., Seto, T., Moteki, N., Koike, M., Oshima, N., Adachi, K., Kita, K., Takami, A., and Kondo, Y.: Enhanced new particle formation above the marine boundary layer over the Yellow Sea: Potential impacts on cloud condensation nuclei, J. Geophys. Res.: Atmos., 125, e2019JD031448, https://doi.org/10.1029/2019JD031448, 2020.

Williamson, C. J., Kupc, A., Axisa, D., Bilsback, K. R., Bui, T., Campuzano-Jost, P., Dollner, M., Froyd, K. D., Hodshire, A. L., Jimenez, J. L., Kodros, J. K., Luo, G., Murphy, D. M., Nault, B. A., Ray, E. A., Weinzierl, B., Wilson, J. C., Yu, F., Yu, 485    P., Pierce, J. R., and Brock, C. A.: A large source of cloud condensation nuclei from new particle formation in the tropics, Nature, 574, 399-403, https://doi.org/10.1038/s41586-019-1638-9, 2019.

Xia, D., Chen, J., Yu, H., Xie, H., Wang, Y., Wang, Z., Xu, T., and Allen, D. T.: Formation Mechanisms of Iodine–Ammonia Clusters in Polluted Coastal Areas Unveiled by Thermodynamics and Kinetic Simulations, Environ. Sci. Technol, 54, 9235-9242, https://doi.org/10.1021/acs.est.9b07476, 2020.

490    Yao, L., Garmash, O., Bianchi, F., Zheng, J., Yan, C., Kontkanen, J., Junninen, H., Mazon, S. B., Ehn, M., Paasonen, P., Sipilä, M., Wang, M., Wang, X., Xiao, S., Chen, H., Lu, Y., Zhang, B., Wang, D., Fu, Q., Geng, F., Li, L., Wang, H., Qiao, L., Yang, X., Chen, J., Kerminen, V.-M., Petäjä, T., Worsnop, D. R., Kulmala, M., and Wang, L.: Atmospheric new particle formation from sulfuric acid and amines in a Chinese megacity, Science, 361, 278-281, https://doi.org/10.1126/science.aao4839, 2018.

Yu, H., Ren, L., Huang, X., Xie, M., He, J., and Xiao, H.: Iodine speciation and size distribution in ambient aerosols at a 495    coastal new particle formation hotspot in China. Atmos. Chem. Phys., 19(6), 4025-4039, https://doi.org/10.5194/acp-19-4025-2019, 2019.

Yu, F. and Luo, G.: Simulation of particle size distribution with a global aerosol model: contribution of nucleation to aerosol and CCN number concentrations, Atmos. Chem. Phys., 9, 7691-7710, https://doi.org/10.5194/acp-9-7691-2009, 2009.

Zhang, J. and Dolg, M.: ABCluster: the artificial bee colony algorithm for cluster global optimization, Phys. Chem. Chem. 500    Phys., 17, 24173-24181, https://doi.org/10.1039/c5cp04060d, 2015.

Zhang, R.: Atmospheric science. Getting to the critical nucleus of aerosol formation, Science, 328, 1366-1367, https://doi.org/10.1126/science.1189732, 2010.

Zheng, G., Wang, Y., Wood, R., Jensen, M. P., Kuang, C., McCoy, I. L., Matthews, A., Mei, F., Tomlinson, J. M., Shilling, J. E., Zawadowicz, M. A., Crosbie, E., Moore, R., Ziemba, L., Andreae, M. O., and Wang, J.: New particle formation in the 505    remote marine boundary layer, Nat. Commun., 12, 1-10, https://doi.org/10.1038/s41467-020-20773-1, 2021.